Materials and Design 67 (2015) 501–508

Contents lists available at ScienceDirect

Materials and Design

journal homepage: www.elsevier.com/locate/matdes

Failure modes in high strength and stiffness to weight scaffolds produced by Selective Laser Melting

Timothy B. Sercombe [a,*], Xiaoxue Xu [a,1], V.J. Challis [b], Richard Green [c], Sheng Yue [c], Ziyu Zhang [d], Peter D. Lee [c,*]

[a] School of Mechanical and Chemical Engineering, The University of Western Australia, Perth, WA 6009, Australia
[b] School of Mathematics & Physics, The University of Queensland, St Lucia, QLD 4072, Australia
[c] School of Materials, The University of Manchester, Manchester M13 9PL, UK
[d] Department of Materials, Prince Consort Road, Imperial College London, London SW7 2BP, UK

ARTICLE INFO

Article history:
Received 24 June 2014
Accepted 23 October 2014
Available online 4 November 2014

Keywords:
Selective Laser Melting
X-ray computed tomography
Titanium alloys
Porous material
Finite-element analysis

ABSTRACT

The production of porous scaffold structures using additive manufacturing is becoming widespread, however a detailed understanding of the scaffold failure mechanisms is lacking. In this research, Selective Laser Melting (SLM) is used to produce Ti–6Al–4V scaffold structures consisting of a regular array of unit cells previously designed using topology optimisation. Interrupted compression testing and subsequent X-Ray Micro Tomography (XMT) characterisation is used to study the deformation and failure of the scaffolds for a range of solid fractions. Further, the XMT data of the unloaded scaffolds is used to generate meshes for finite element analysis which allowed direct comparison of desired and as built behaviour. Likely failure sites predicted from the finite element analysis compare favourably with the experimentally observed ones. Failure is initiated in areas that exhibit the greatest tensile stress, while the onset of the commonly observed layered failure occurs afterwards. The XMT of the unloaded scaffolds also highlights the inaccuracies in the SLM build process, which contributes to stress concentrations in the horizontal arms within the scaffolds. The results indicate that although the strength of the topology optimised structures is very high, further refinement in both the unit cell design and build quality would further increase the strength.

1. Introduction

The use of porous materials for regenerative medicine is attracting increasing interest due to the ability to control the stiffness [1,2] of the device as well as promote the in growth of bone [3]. In load bearing applications, polymers and ceramics do not possess the requisite mechanical strength and toughness to survive the *in vivo* loading and therefore metals and their alloys have become the material of choice [4].

The relatively low modulus of titanium, along with its excellent corrosion resistance and very high specific strength, has resulted in it being widely favoured for bone replacement applications [4,5]. Even so, Ti has a modulus which is at least an order of magnitude larger than bone. Mismatch of moduli between the biomaterial and surrounding bone can cause stress shielding in the bone, which eventually leads to bone resorption, and has been identified as a major causal factor of implant loosening [3,6]. The modulus of a material can be decreased by introducing porosity, which, provided it is interconnected, can have the additional desired effect of promoting bone in-growth [7–9], along with easy diffusion of nutrients to and waste from the implant [10,11].

There are a number of methods to produce porous titanium components (see [12–14] for recent reviews). Of these methods, only additive manufacturing ("3D printing") techniques enables the fabrication of anatomically-shaped scaffolds with complex internal architectures, allowing precise control of the porosity (including pore size, shape and interconnectivity) and therefore stiffness.

The mechanical strength of porous materials is determined largely by the characteristics of the pores – namely their size, volume fraction and shape [15], as these dictate the size of the load bearing struts. There have been a number of methods used to predict the mechanical behaviour of porous solids. Gibson and Ashby [16] have developed a micromechanical model to predict the strength of foams based on the physical characteristics such as relative

* Corresponding authors. Tel.: +61 8 6488 3124 (T.B. Sercombe), +44 1235 567789 (P.D. Lee).
E-mail addresses: tim.sercombe@uwa.edu.au (T.B. Sercombe), peter.lee@manchester.ac.uk (P.D. Lee).
[1] Present address: Department of Chemistry and Biomolecular Sciences, Macquarie University, Sydney, NSW 2109, Australia.

http://dx.doi.org/10.1016/j.matdes.2014.10.063
0261-3069/

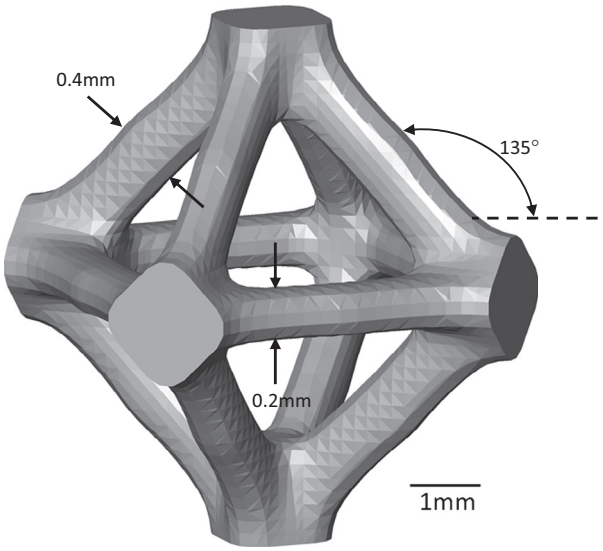

Fig. 1. The optimised unit cell at a 10% solid fraction. The samples were built using an array of 3 × 3 × 3 cells at 7%, 10% and 15% solid fractions. All struts have the same dimensions.

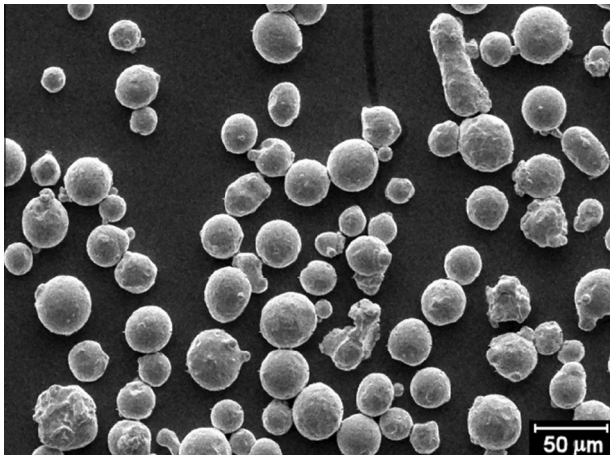

Fig. 2. Scanning electron image of the Ti–6Al–4V powder.

density, the nature of the porosity (i.e. open or closed) and the material properties of the metal. Predictions using continuum micromechanics were subsequently developed [17] to overcome some of the limitations of the Gibson–Ashby models (namely assumptions of uniform porosity, idealised smooth struts and the absence of any axial or shear displacement of the foam edges during loading). A third approach has been to use finite element modelling (FEM) of the three dimensional (3D) structure and has been used to predict the compressive behaviour of bone [18], titanium [19–21], aluminium [22–26] and bioactive glasses [27]. This modelling work usually has been accompanied by X-Ray Micro Tomography (XMT), which can be used to quantify the 3D microstructure, generate the required FEM meshes and directly

Table 2
Laser parameters used.

Parameter	On powder setting		On solid setting	
	Contour	Fill	Contour	Fill
Laser power (W)	100	140	140	200
Point distance (µm)	120	120	120	100
Exposure time (µs)	80	80	80	80
Scan speed (mm/s)	1500	1500	1500	1250

Table 3
Comparison between the nominal, CAD and actual as fabricated solid fraction for the scaffolds used.

Nominal solid fraction (%)	CAD model solid fraction (%)	Fabricated solid fraction (%)
7	6.5	7.4 ± 0.3
10	9.5	10.5 ± 0.3
15	14.7	15.4 ± 0.4

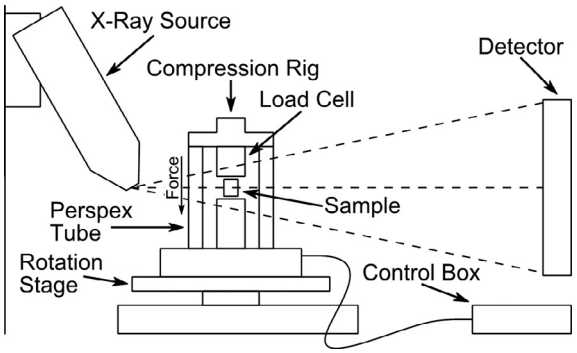

Fig. 3. Schematic of the in situ compression rig. The samples were held at constant strain while the XMT scan was performed.

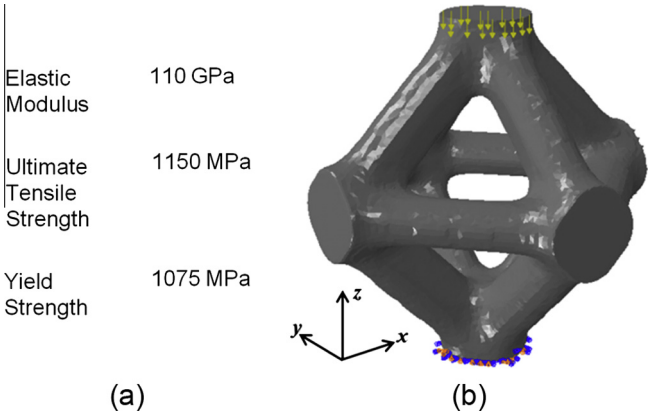

Fig. 4. Bulk properties used in the finite element analysis (a) and the constraints and loading applied (b). The yellow arrows indicate constant load. The orange and blue marks indicate the constraints applied: in the bottom *xy*-plane there is a symmetry restraint in *z* translation, *x* rotation and *y* rotation. The points where the loading and constraints are applied are equally spaced around the surface of the structure. (For interpretation of the references to colour in this figure legend, the reader is referred to the web version of this article.)

Table 1
Selected characteristics of the Ti–6Al–4V powder used in this work.

Powder composition (wt%)						Powder size (µm)			Flow rate (s/50g)	Apparent density (%)
Ti	Al	V	O	N	Fe	d_{10}	d_{50}	d_{90}	15.6	57.5
Bal	6.25	4.04	0.14	0.02	0.22	25.6	37.5	51.1		

study the deformation behaviour [21,28–30] and flow properties [31] and bone in growth [32] into porous solids. This provides insights into the failure mechanisms, especially the prediction of the most vulnerable localised regions.

Recently [2] we have shown the advantage of combining topology optimisation and Selective Laser Melting (SLM) to produce structures with exceptionally high strength and stiffness to weight. However, we do not understand the deformation or failure mechanisms of these structures, which is hindering our ability to improve the design further. In this work, we have studied the failure of topology optimised structures [1,33] using interrupted compression testing and XMT characterisation, allowing the direct comparison of the desired properties and failure mechanisms to those actually achieved.

2. Experimental details

2.1. Part manufacture

In this work, scaffolds were created from a unit cell that was designed using topology optimisation [1,33] at three different nominal solid fractions, 7%, 10% and 15%. The base unit cell of the 10% solid fraction is shown in Fig. 1. These unit cells have exceptionally high strength and stiffness to weight ratio [2].

Structures consisting of $3 \times 3 \times 3$ unit cells, 3.333 mm in size (overall size $10 \times 10 \times 10\ mm^3$), were manufactured using Selective Laser Melting (SLM) on a Realizer SLM100 machine (Borchen, Germany). The Ti–6Al–4V powder that was used was obtained from TLS Technik, Germany. A scanning electron image (Zeiss

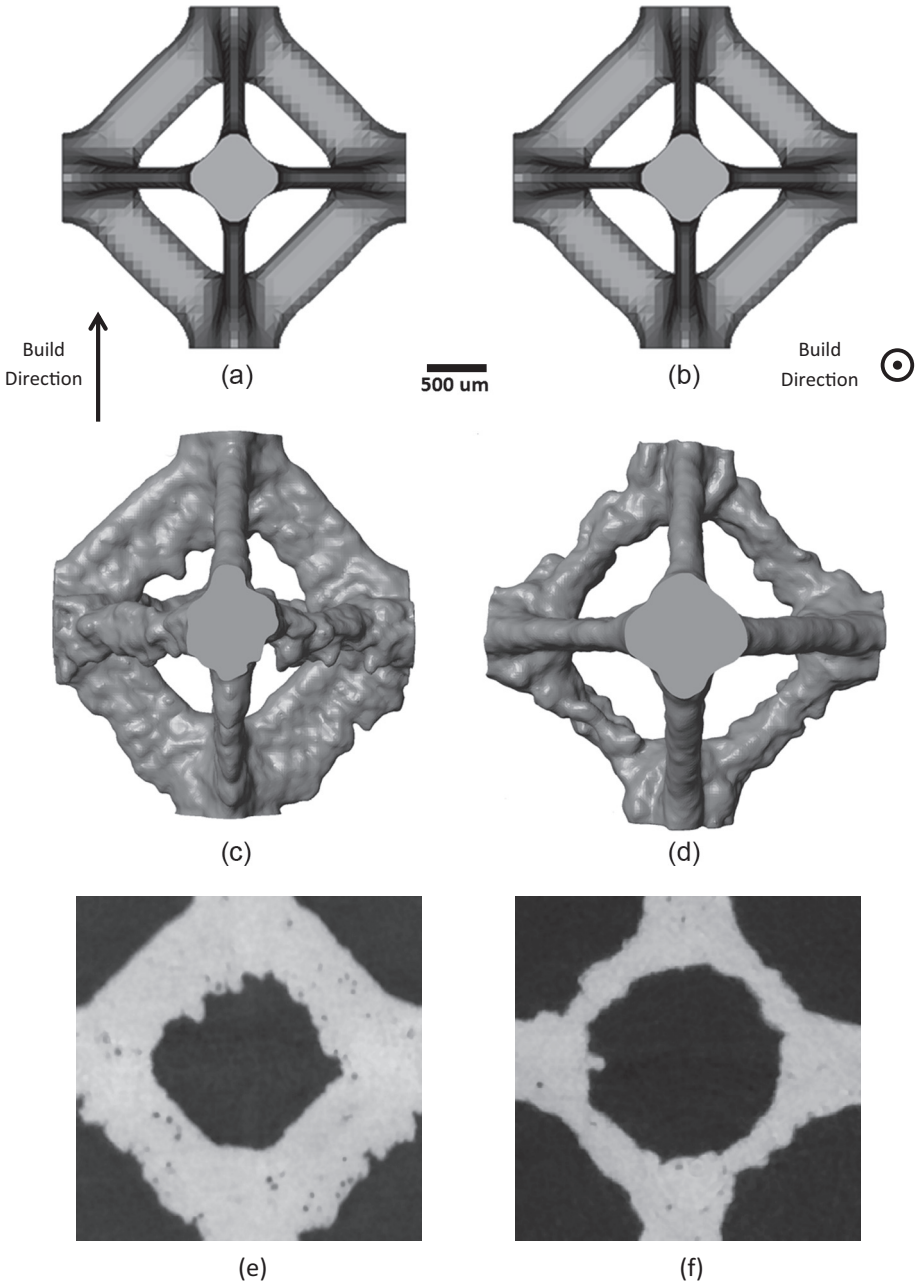

Fig. 5. Comparison between the CAD file ((a), (b)), actually built unit cell ((c), (d)) and the central slice ((e) and (f)) for the 10% solid fraction scaffold. The side view is shown in (a), (c) and (e), and the top view in (b), (d) and (f). It is apparent comparing (a) and (c) that there is significantly greater surface roughness on the downward facing surfaces, while the horizontal arms (shown in (d)) are smaller than in the model, they are essentially fully dense and integral.

1555 VP-FESEM, Jena, Germany) of the powder is shown in Fig. 2 and the important characteristics of the powder are summarised in Table 1. The composition was measured using inductively coupled plasma atomic emission spectroscopy (ICP-AES) by Spectrometer Services (Melbourne, Australia), the particle size using a Malvern Microsizer Plus (Worcestershire, UK) and the flow and apparent density according to Metal Powder Industries Federation Standard 03 and 04 [34], respectively. The theoretical density of the alloy was taken to be 4.43 g/cm^3.

The SLM processing parameters used are summarised in Table 2. Each slice was divided into regions that were "on solid" (that is contained at least one layer of solid beneath them) or "on powder" (which contained only powder below, such as would occur on the overhangs of downward facing surfaces). Determination of the "on powder" and "on solid" areas was performed using the Realizer software. The control of the laser speed is achieved through the independent setting of a point distance (d) and exposure time at each point (t) and therefore the overall laser speed is d/t. In all cases the parts were built on a commercially pure Ti substrate plate, using an Ar atmosphere that contained <1000 ppm of oxygen. The layer thickness, laser scan spacing and laser offset were kept constant at 50, 100 and 60 μm, respectively. The direction of the laser was rotated 90° between layers and was always parallel to the edge of the scaffold structures. After building, the parts were removed from the substrate, the support structure was removed and the parts cleaned by glass bead blasting and then compressed air. The dimensions of the scaffold and weight were then measured to an accuracy of 10 μm and 1 mg respectively in order to calculate the density and therefore solid fraction. A comparison between the nominal solid fraction with that of the CAD model and the as-built scaffold structures is shown in Table 3.

2.2. X-Ray Micro Tomography

In situ X-Ray Micro Tomography (XMT) was used in conjunction with interrupted compression testing to study the compressive deformation of the scaffolds. The sample was loaded into a Deben rig (St Edmunds, UK), with a maximum load rating of 10kN and compressed at a constant strain rate of 0.05 mm/min. The loading direction was parallel to the build direction of the sample. Prior to, and periodically during compression, the sample was held at a constant strain, and a 360° tomographic scan performed. The XMT was performed using a Nikon Metris 225 (Nikon Metrology, UK) at 130 kV and 300μA with a voxel size of 24.5 μm. Projections (2000, 250 ms exposure time) were collected on a 2 k × 2 k charge-coupled device detector. XMT images were then reconstructed from these projections using a cone beam back-projection algorithm. A schematic of the experimental set up is shown in Fig. 3.

2.3. FEA analysis

Volumes of individual unit cells with different solid fractions (7%, 10% and 15%) from the XMT scans were segmented and meshed in a commercial FEM meshing package, ScanIP (Simpleware Ltd., UK). The FEM meshes were then imported into the FEM analysis package Abaqus/CAE (Dassault Systemes Simulia Corp., USA). Fig. 4 shows the schematic of the 3D FEA model and the boundary conditions applied in the simulation, along with the material bulk properties. The modulus of the bulk material was determined using separately produced, machined rectangular samples (48 × 11 × 5 mm^3) built parallel to the horizontal axis of the machine, using an impulse excitation technique on a Grindosonic™ instrument (Heverlee, Belgium). These bars were subsequently machined into tensile samples (gauge length 6 × 4 × 15 mm^3), and tested on an Instron 5982 (Norwood, MA, USA), using a 10 mm extensometer and at a cross head speed of 1 mm/min. The testing direction was normal to the build direction. The top surface node set was assigned a constant load along z-direction and the bottom surface node was restricted from moving in the z-direction. Note that due to the different strengths of the various solid factions, the force was scaled with the solid fraction, i.e. a load ratio of 2:5:10 was used for the 7%, 10% and 15% solid fractions respectively. In addition to the single unit cells, FEA analysis on the ideal unit cell (model) and a 3 × 3 × 3 volume of the actual 10% solid fraction structure were performed.

3. Results

The structure of the central cell from the 10% solid fraction scaffold is compared to the computer model from which it was built in Fig. 5. It is clear that the geometrical reproduction of the model is not perfect. In particular, there are localised increases in the size ("Z-growth") of the vertical members (see Fig. 5(c)) resulting in high surface roughness of the downwards facing surfaces. In contrast, upwards facing surfaces are relatively smooth and well defined. For the horizontal members, shown in Fig. 5(d), the thickness is much less than the model and also contains significant variability and roughness. Nonetheless, as shown in Fig. 5(e) and

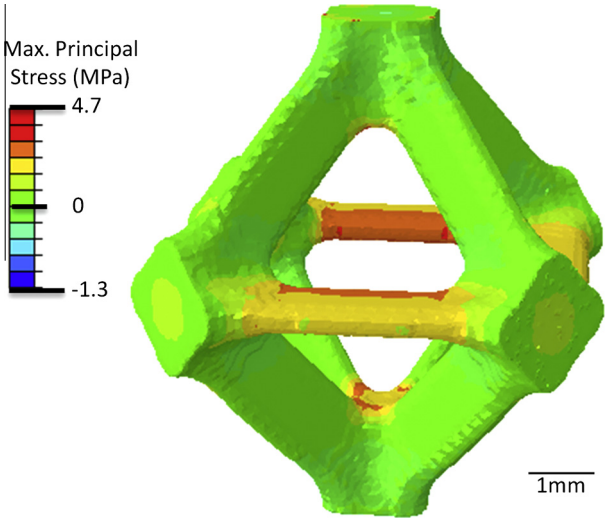

Fig. 6. Finite element analysis of the unit cell. It is apparent that the horizontal arms carry the tensile load and the vertical one, compression.

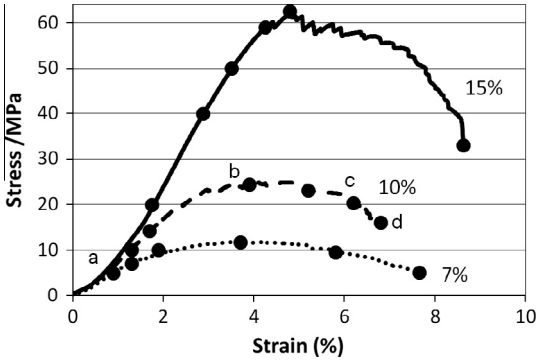

Fig. 7. Typical stress strain curves for optimised structures at the solid fractions used as acquired on an Instron material testing machine. The overlaid dots indicate the equivalent position that XMT scans were performed. The numbers indicate the nominal solid fraction of the structure (see Table 3).

(f), both the horizontal and vertical arms are solid and contain only a low level of porosity. FEA analysis of the ideal unit cell, Fig. 6, reveals that under uniaxial compression, the horizontal arms carry tensile loading, while the vertical arms are loaded in compression.

The mechanical behaviour of the scaffolds at the various solid fractions is shown in Fig. 7 together with the points at which the compression test was interrupted for scanning. The general shape of the stress strain curve is similar to that of a conventional bulk material.

Progressive deformation of the 10% solid fraction scaffold at points (a)–(d) in Fig. 7 is shown in Fig. 8. This Figure shows that gradual deformation of the vertical sections occurs prior to shear failure at an angle of 45° to the applied load. Fig. 8(e) is a 3D rendering of the final failed structure. Similar deformation characteristics were observed in all solid fraction samples.

The initial failure site for the three solid fractions was identified in the reconstructed XMT data from the point just beyond the peak load (shown in Fig. 7). These failure sites are indicated on the isolated individual unit cell in which they occurred in Fig. 9 alongside the stress distribution as predicted by the FEA. For all solid fractions, the first failure occurred in the horizontal arms and the exact failure location aligned with regions of high tensile stress due to build variations as predicted by the FEA.

The locations where the scaffold collapses can be seen in Fig. 10. This is for the central layer of the 10% solid fraction structure at stress 'c' in Fig. 7, well beyond the peak load. It is apparent that failure progressed via multiple fracturing of the horizontal arms (Fig. 10(a)), with the vertically aligned members remaining intact, Fig. 10(c). The site of the fractures is also indicated on the FEA results in Fig. 10(b). Similar to what was shown in Fig. 9, there is a very close

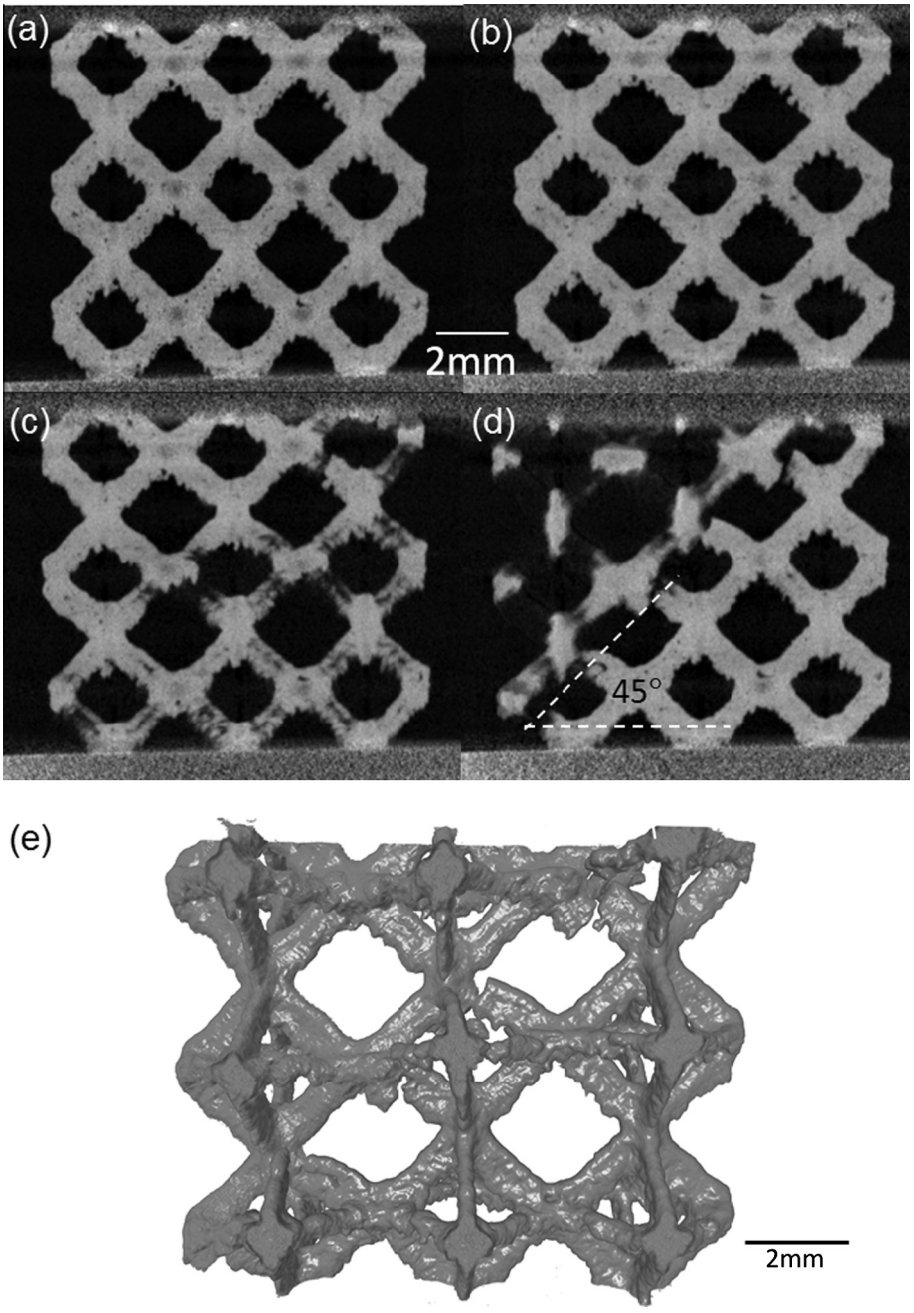

Fig. 8. Compression of a central slice through the 10% optimised structure at the points (a) to (d) shown in Fig. 4. The central plane of unit cells after compression at (d) is rendered in 3D in (e).

correlation between the high stress areas and location of the failures. The failure of the horizontal arms prior to the vertical arms occurred on all layers of the scaffold and for all three solid fractions.

4. Discussion

The geometric freedom afforded by advanced manufacturing technologies such as SLM facilitates the production of previously unachievable geometries. However, the accuracy of the reproduction of the structure is limited by the fact that the process is powder based and also by the local instabilities in the melt pool that can form during the scanning of the laser across the powder bed. At high laser energies the cylindrical melt pool can become unstable due to rapid convective motion known as thermo-capillary or Marangoni flow [35–38]. This instability causes the melt pool to break up into large non-continuous droplets, an effect usually called "balling". If the energy density is too low however, insufficient melting creates a smaller melt pool and if the length to diameter ratio of this melt pool becomes larger than π, small balls form, commonly thought to occur as a result of Rayleigh instability [35,39,40]. Between these two extremes, smooth regular scan tracks form. However even these can form irregularities due to localised changes in the thermal conditions [41]. Of particular concern are overhangs or unsupported horizontal surfaces. In these regions, the laser scans across powder that does not have any solid material below. During SLM, heat conduction through the underlying solid causes rapid cooling of the laser scanned material and therefore higher laser energies are required to compensate [35]. Since loose powder has significantly lower thermal conductivity than solid metal, a lower energy is required to fully melt the powder. The use of the same energy will cause superheating of the melt pool, diffusion of the heat into the underlying powder, and melting of powder from beyond the layer being scanned. Consequently, the scanning strategy employed divided each slice in to areas which have solid beneath ("on solid") and areas which have powder beneath ("on powder"). A different set of parameters were used for each area (Table 2). Despite this lowered energy, it is apparent that on downwards facing surfaces (see Fig. 5(b)) the laser energy penetrates beyond the layer being scanned and is sufficient to melt, or partially melt, the powder, causing surface roughness and growth in the *z*-direction. However this penetration is not consistent, which may be a result of localised variability in the powder packing and hence thermal conductivity.

Unsupported horizontal arms can also be problematic to build via SLM. Residual stresses and aforementioned variability in powder packing can result in the formation of unstable melt tracks, which causes the significant surface roughness (Fig. 5(c)). Fig. 5 also shows that the horizontal arms are thinner than the model, possibly as a result of contraction of the liquid pool as it solidifies, which would act to increase the stress levels in these sections.

Despite the inaccuracies in the build, this unit cell possesses exceptional strength and stiffness to weight [2]. However, mechanism(s) by which these structures fail has not been investigated, which prevents further refinement of the design. Failure of random porous structures, such as foams, tends to occurs via collapse of the entire horizontal layer containing the weakest strut soon after yielding [22,42,43]. As a result of this failure mechanism, a rapid drop in the strength often occurs soon after yielding. This is due to the concentration of the stress in the material surrounding the failure site causing subsequent localised collapse of the structure. Similar behaviour has been reported in Selective Laser or Electron Beam Melted scaffold structures [9,44–47], with a sudden drop in the stress occurring immediately after yielding and where localised failure along an angle of 45° to the applied load is often observed [9,46,47]. However, it is apparent from Fig. 7, that these structures

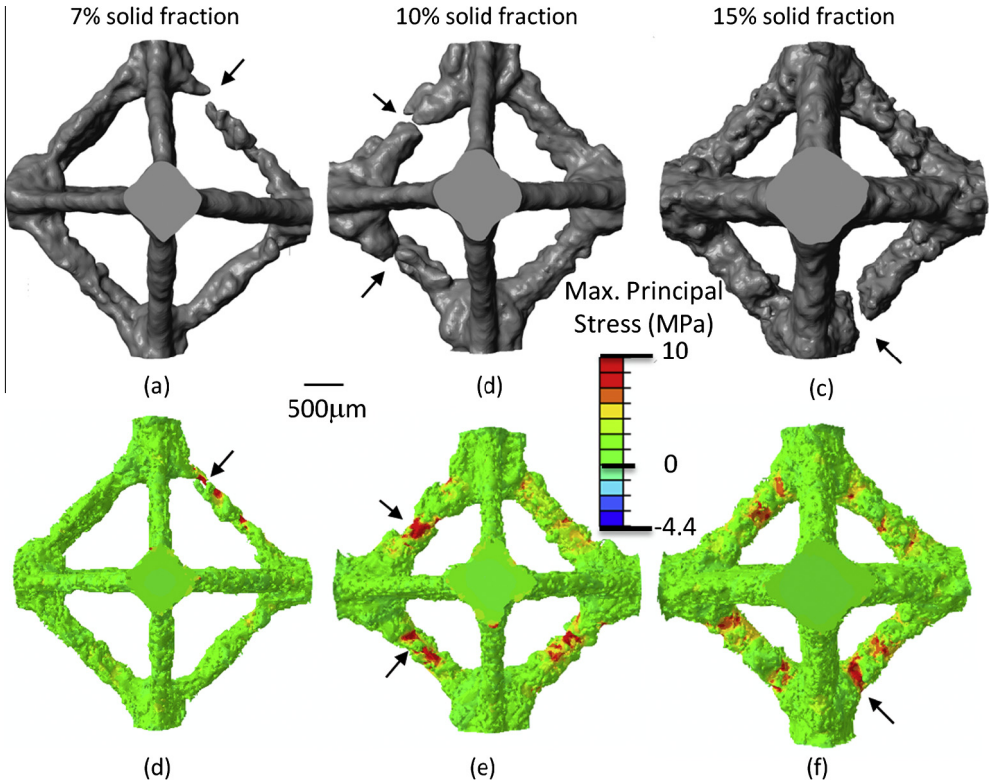

Fig. 9. Comparison between the (a)–(c) first failure site and (d)–(f) FEA of the starting structure for the three volume fractions used. In all cases, the initial failure site occurred in the horizontal arms and was in an area that the FEA predicts as having high tensile stress. Images are of the top view.

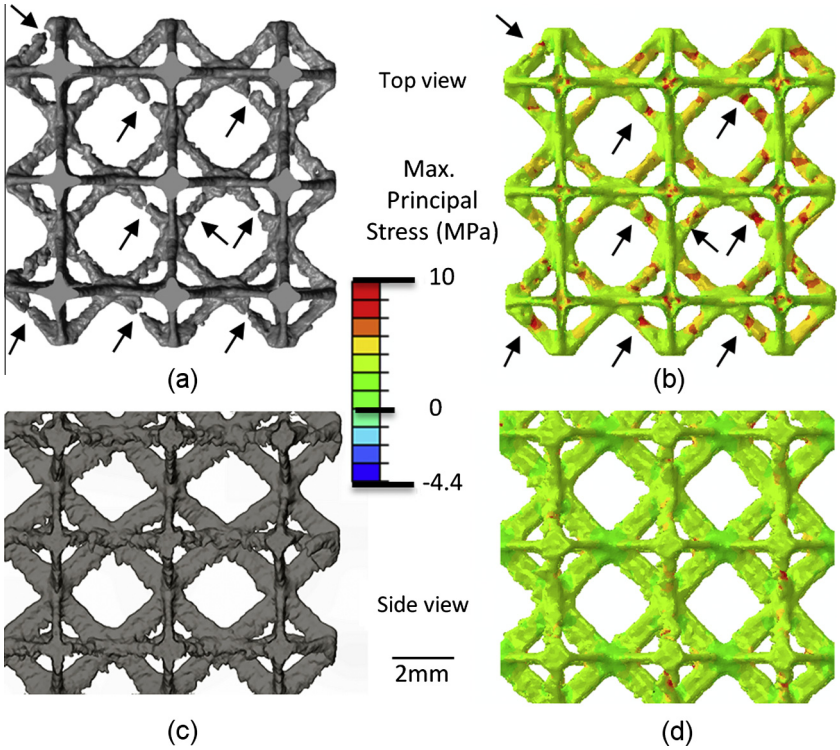

Fig. 10. XMT and corresponding FEA of the central layer of unit cells for the 10% solid fraction scaffold. This scaffold has been loaded well beyond the peak load (to point C in Fig. 6) and exhibits multiple fractures of the horizontal arms (arrowed). The top view is shown in (a) and (b) and the side view in (c) and (d). It is apparent that the failure sites are strongly correlated with the high stress regions in the FEA, which are also indicated with arrows.

exhibit very different failure behaviour and behave much more like a bulk material – that is beyond yielding, the load carrying capacity of the structure continues to increase. Therefore it appears that a different failure mechanism is in operation.

For all solid fractions studied, failure first occurred in the horizontally aligned struts, Fig. 9(a–c). These arms carry tensile loading (Fig. 6). However, the reduced cross sectional area and significant surface roughness causes the peak stress to be approximately twice that predicted in the ideal unit cell, Fig. 9(d–f). Hence it is quite clear that the initial failure not only occurs in the struts that are loaded in tension, but is also located at the regions of high stress concentration due to build variations.

Subsequent to the first failure, continued loading results in progressive fracture of these tension loaded, horizontal struts, Fig. 10(a), while the vertically aligned members, which are mostly in compression, remain intact, Fig. 10(c). Similar to the initial failure, all the failure sites of the struts occurred at the location of high tensile stress as predicted in the FEA, Fig. 10(b). Both the site of first failure and also the way in which the failure propagates did not change with the solid fraction of the structure. In all cases, the horizontal arms fail first, with continued load carrying ability being maintained by the vertical members. Final collapse of the structure occurs as a result of the fracturing/collapse of the vertical arms, which occurs at 45° to the stress direction, Fig. 8(d) and (e). Once the horizontal strut arms have fractured, the scaffold structure becomes similar to an octahedral structure, which is known to fail in a localised shear band in both static [47] and fatigue loading [48]. Hence it is apparent that these structures are failing in a way that is very different from the "floor-by-floor" mechanism often observed in porous foams. The result of this is that the initial failure of the scaffold does not cause a large drop in the load carrying capacity of the structure once the yield point is exceeded, which increases the damage tolerance of the design.

5. Conclusions

In this work, we have coupled in situ compression testing XMT with FEA to investigate the failure mechanisms of high strength and stiffness to weight scaffold structures, over a range of solid fractions. From this work, we have made the following conclusions:

- It is apparent that the failure of these structures first occurs in the struts that carry the tensile load. Further, failure occurred at the sites that FEA predicted to have high localised stress due to poor build quality. Therefore, by improving the build quality (to minimise the high surface roughness), it may be possible to improve the load carrying capacity of these high strength scaffolds even further. This highlights the feedback/optimisation loop that XMT facilitates, especially when coupled to in situ loading capabilities. The scale and complexity of these structures means that both optical and electron microscopy are not effective characterisation techniques.
- By combining XMT and FEA, the failure site(s) of the scaffolds can be predicted prior to physical testing and therefore can be used as an important tool in the evaluation of new scaffold designs.
- The failure mode was very different to the classical floor-by-floor mechanism of traditional foam materials and, as a result, significant load carrying capacity was maintained even after the onset of strut failure. Only once all the horizontal arms had failed, was a more traditional failure mode observed, with a sheer band forming at 45°.

Acknowledgements

This work was made possible by the facilities and support provided by the Manchester X-ray Imaging Facility and the Research

Complex at Harwell, funded in part by the EPSRC (EP/I02249X/1) and the Australian Research Council's Discovery Projects funding scheme (project number DP110101653).

References

[1] Challis VJ, Roberts AP, Grotowski JF, Zhang L-C, Sercombe TB. Prototypes for bone implant scaffolds designed via topology optimization and manufactured by solid freeform fabrication. Adv Eng Mater 2010;12:1106–10.

[2] Challis VJ, Xu X, Zhang LC, Roberts AP, Grotowski JF, Sercombe TB. High specific strength and stiffness structures produced using selective laser melting. Mater Des 2014;63:783–8.

[3] Robertson DM, Pierre LSt, Chahal R. Preliminary observations of bone ingrowth into porous materials. J Biomed Mater Res 1976;10(3):335–44.

[4] Niinomi M. Recent metallic materials for biomedical applications. Metall Mater Trans A 2002;33(3):477–86.

[5] Wang K. The use of titanium for medical applications in the USA. Int Symp Metall Technol Ti Alloys 1996;213(1–2):134–7.

[6] Head WC, Baulk DJ, Emersom RH. Titanium as the material of choice for cementless femoral components in total hip arthroplasty. Clin Orthop Relat Res 1995;311:85.

[7] Hulbert SF, Morrison SJ, Klawitter JJ. Tissue reaction to three ceramics of porous and non-porous structures. J Biomed Mater Res 1972;6(5):347–74.

[8] Holy CE, Shoichet MS, Davies JE. Engineering three-dimensional bone tissue in vitro using biodegradable scaffolds: investigating initial cell-seeding density and culture period. J Biomed Mater Res 2000;51(3):376–82.

[9] Yang L, Harrysson O, West H, Cormier D. Compressive properties of Ti–6Al–4V auxetic mesh structures made by electron beam melting. Acta Mater 2012;60:3370–9.

[10] Yue S, Lee PD, Poologasundarampillai G, Jones JR. Evaluation of 3-D bioactive glass scaffolds dissolution in a perfusion flow system with X-ray microtomography. Acta Biomater 2011;7:2637–43.

[11] Murphy CM, O'Brien FJ. Understanding the effect of mean pore size on cell activity in collagen-glycosaminoglycan scaffolds. Cell Adhes Migr 2010;4(3):377–81.

[12] Singh R, Lee PD, Dashwood RJ, Lindley TC. Titanium foams for biomedical applications: a review. Mater Technol 2010;25:127–36.

[13] Dunand DC. Processing of titanium foams. Adv Eng Mater 2004;6(6):369–76.

[14] Ryan G, Pandit A, Apatsidis DP. Fabrication methods of porous metals for use in orthopaedic applications. Biomaterials 2006;27(13):2651–70.

[15] Davies GJ, Zhen S. Metallic foams: their production, properties and applications. J Mater Sci 1983;18(7):1899–911.

[16] Gibson LJ, Ashby MF. Cellular solids: structure and properties. Cambridge University Press; 1999.

[17] Zaoui A. Continuum micromechanics: survey. J Eng Mech 2002;128(8):808–16.

[18] Crawford RP, Cann CE, Keaveny TM. Finite element models predict in vitro vertebral body compressive strength better than quantitative computed tomography. Bone 2003;33(4):744–50.

[19] Shen H, Brinson LC. Finite element modeling of porous titanium. Int J Solids Struct 2007;44(1):320–35.

[20] Thelen S, Barthelat F, Brinson LC. Mechanics considerations for microporous titanium as an orthopedic implant material. J Biomed Mater Res – Part A 2004;69(4):601–10.

[21] Singh R, Lee PD, Lindley TC, Kohlhauser C, Hellmich C, Bram M, et al. Characterization of the deformation behavior of intermediate porosity interconnected Ti foams using micro-computed tomography and direct finite element modeling. Acta Biomater 2010;6:2342–51.

[22] Bart-Smith H, Bastawros AF, Mumm DR, Evans AG, Sypeck DJ, Wadley HNG. Compressive deformation and yielding mechanisms in cellular Al alloys determined using X-ray tomography and surface strain mapping. Acta Mater 1998;46:3583–92.

[23] Ohgaki T, Toda H, Kobayashi M, Uesugi K, Kobayashi T, Niinomi M, et al. In-situ high-resolution X-ray CT observation of compressive and damage behaviour of aluminium foams by local tomography technique. Adv Eng Mater 2006;8:473–5.

[24] Toda H, Ohgaki T, Uesugi K, Kobayashi M, Kuroda N, Kobayashi T, et al. Quantitative assessment of microstructure and its effects on compression behavior of aluminum foams via high-resolution synchrotron X-ray tomography. Metall Mater Trans A 2006;37:1211–9.

[25] Watson IG, Lee PD, Dashwood RJ, Young P. Simulation of the mechanical properties of an aluminum matrix composite using X-ray microtomography. Metall Mater Trans A 2006;37:551–8.

[26] Zhang Q, Lee PD, Singh R, Wu G, Lindley TC. Micro-CT characterization of structural features and deformation behavior of fly ash/aluminum syntactic foam. Acta Mater 2009;57:3003–11.

[27] Jones JR, Lee PD, Hench LL. Hierarchical porous materials for tissue engineering. Philos Trans Royal Soc A 1838;2006(364):263–81.

[28] Hangai Y, Takahashi K, Yamaguchi R, Utsunomiya T, Kitahara S, Kuwazuru O, et al. Nondestructive observation of pore structure deformation behavior of functionally graded aluminum foam by X-ray computed tomography. Mater Sci Eng, A 2012;556:678–84.

[29] Michailidis N, Stergioudi F, Omar H, Papadopoulos D, Tsipas DN. Experimental and FEM analysis of the material response of porous metals imposed to mechanical loading. Colloids Surf A 2011;382:124–31.

[30] Hangai Y, Kato H, Utsunomiyav T, Kitahara S, Kuwazuru O, Yoshikawa N. Effects of porosity and pore structure on compression properties of blowing-agent-free aluminum foams fabricated from aluminum alloy die castings. Mater Trans 2012;53:1515–20.

[31] Zhang Z, Jones D, Yue S, Lee PD, Jones JR, Sutcliffe CJ, et al. Hierarchical tailoring of strut architecture to control permeability of additive manufactured titanium implants. Mater Sci Eng C 2013;33:4055–62.

[32] Zhang Z, Yuan L, Lee PD, Jones E, Jones JR. Modeling of time dependent localized flow shear stress and its impact on cellular growth within additive manufactured titanium implants. J Biomed Mater Res – Part B 2014;102:1689–99.

[33] Challis VJ, Roberts AP, Wilkins AH. Design of three dimensional isotropic microstructures for maximized stiffness and conductivity. Int J Solids Struct 2008;45(14–15):4130–46.

[34] Standard Test Methods for Metal Powders and Powder Metallurgy Products. Princeton, New Jersey USA: Metal Powder Industries Federation; 2009

[35] Yadroitsev I, Bertrand P, Smurov I. Parametric analysis of the selective laser melting process. Appl Surf Sci 2007;253(19):8064–9.

[36] Gu DD, Meiners W, Wissenbach K, Poprawe R. Laser additive manufacturing of metallic components: materials, processes and mechanisms. Int Mater Rev 2012;57:133–64.

[37] Lee PD, Quested PN, McLean M. Modelling of Marangoni effects in electron beam melting. Philos. Trans. Royal Soc. Lond. A 1998;356(1739):1027–43.

[38] Rombouts M, Kruth JP, Froyen L, Mercelis P. Fundamentals of Selective Laser Melting of alloyed steel powders. CIRP Annals – Manuf Technol 2006;55:187–92.

[39] Gusarov AV, Yadroitsev I, Bertrand P, Smurov I. Heat transfer modelling and stability analysis of selective laser melting. Appl Surf Sci 2007;254:975–9.

[40] Childs THC, Hauser C, Badrossamay M. Mapping and modelling single scan track formation in direct metal selective laser melting. CIRP Annals – Manuf Technol 2004;53(1):191–4.

[41] Ciurana J, Hernandez L, Delgado J. Energy density analysis on single tracks formed by selective laser melting with CoCrMo powder material. Inter J Adv Manuf Technol 2013:1–8.

[42] Raj RE, Daniel BSS. Structural and compressive property correlation of closed-cell aluminum foam. J Alloy Compd 2009;467(1–2):550–6.

[43] Ashby MF. Plastic deformation of cellular materials. In: KHJB, Robert WC, Merton CF, Bernard I, Edward JK, Subhash M, editors. Encyclopedia of materials: science and technology. Oxford: Elsevier; 2001. p. 7068–71.

[44] Heinl P, Körner C, Singer RF. Selective Electron Beam Melting Of Cellular Titanium: Mechanical Properties. Adv Eng Mater 2008;10(9):882–8.

[45] Smith M, Guan Z, Cantwell WJ. Finite element modelling of the compressive response of lattice structures manufactured using the selective laser melting technique. Inter J Mech Sci 2013;67:28–41.

[46] Gorny B, Niendorf T, Lackmann J, Thoene M, Troester T, Maier HJ. In situ characterization of the deformation and failure behavior of non-stochastic porous structures processed by selective laser melting. Mater Sci Eng, A 2011;528:7962–7.

[47] Cheng XY, Li SJ, Murr LE, Zhang ZB, Hao YL, Yang R, et al. Compression deformation behavior of Ti–6Al–4V alloy with cellular structures fabricated by electron beam melting. J Mech Behav Biomed Mater 2012;16:153–62.

[48] Li SJ, Murr LE, Cheng XY, Zhang ZB, Hao YL, Yang R, et al. Compression fatigue behavior of Ti–6Al–4V mesh arrays fabricated by electron beam melting. Acta Mater 2012;60:793–802.